Analysis of the x-ray diffraction signal for the α-ϵ transition in shock-compressed iron: Simulation and experiment

J. Hawreliak,[*] J. D. Colvin, J. H. Eggert, D. H. Kalantar, H. E. Lorenzana, and J. S. Stölken

Lawrence Livermore National Laboratory, Livermore, California 94550, USA

H. M. Davies

AWE Aldermaston, Reading, United Kingdom

T. C. Germann, B. L. Holian, K. Kadau, and P. S. Lomdahl

Los Alamos National Laboratory, Los Alamos, New Mexico 87545, USA

A. Higginbotham, K. Rosolankova, J. Sheppard, and J. S. Wark

Department of Physics, Clarendon Laboratory, University of Oxford, Oxford OX1 3PU, United Kingdom

Recent published work has shown that the phase change of shock-compressed iron along the [001] direction does transform to the ϵ [hexagonal close-packed (hcp)] phase similar to the case for static measurements. This article provides an in-depth analysis of the experiment and nonequilibrium molecular dynamics simulations, using x-ray diffraction in both cases to study the crystal structure upon transition. Both simulation and experiment are consistent with a compression and shuffle mechanism responsible for the phase change from body-centered cubic to hcp. Also both show a polycrystalline structure upon the phase transition, due to the four degenerate directions in which the phase change can occur.

PACS number(s): 61.10.Nz, 68.18.Jk, 67.80.Cx, 68.18.Fg

I. INTRODUCTION

It is almost a full century since the start of the Nobel-prize-winning work of Bridgman showing that many crystals transform to new structures under the influence of static pressure.[1] There is a large body of evidence that many pressure-induced phase transitions occur under shock compression, which is remarkable considering that the time scale over which the pressure is applied to the material in shock experiments is many orders of magnitude shorter than in the static experiments. The most well known, and indeed most widely studied of these shock-induced transformations is the α-ϵ transition in iron, where the body-centered cubic (bcc) lattice is thought to transform to hexagonal close packed (hcp), shown in Fig. 1. The significance of this transition in iron is related to the millennia-old importance of iron in the development of human civilization, as well as in geophysics, being the principal element within the earth's core. It is even speculated that the crystalline properties of the earth's core have measurable affects at the surface.[2] However, despite having been studied for several decades, until recently, no direct experimental data about how the atoms can rearrange on such ultrafast time scales existed.[3,4]

The first tentative evidence for the α-ϵ transition under shock conditions came half a century ago, when Walsh reported data on the propagation of high-pressure shock waves in Armco iron[5] that were in disagreement with an extrapolation of Bridgman's original static compressibility measurements:[6] Walsh's measurements implied a compression up to 20% higher than predicted. This discrepancy was explained by Bancroft, Peterson, and Minshall, when they observed a multiple-wave shock structure within a single sample.[7,8] They associated the splitting of the waves with the elastic-plastic response and the subsequent transformation of iron to a different phase. Analysis of the wave profiles implied that the onset of the phase transition occurred at a pressure of 13 GPa. At that time the α-ϵ phase transition in iron was unknown. It was speculated that the inferred transition could be the $\alpha-\gamma$ phase transition (bcc-fcc), which was known to occur at ≈ 1000 K at standard pressure (see Fig. 1), but there was difficulty in believing a solid-solid phase transition could occur on a microsecond time scale.[9]

It was only several years after Minshall's shock-wave work that crystallographic evidence for a bcc-hcp transition at 13 GPa was obtained in static x-ray diffraction experiments by Jamieson and Lawson.[13] This confirmation that a phase transition occurred under static conditions at an (almost) identical pressure to that deduced from the earlier shock-wave measurements has long been hailed as one of the major triumphs in the field of shock-wave physics. It has been assumed ever since that the transition associated with
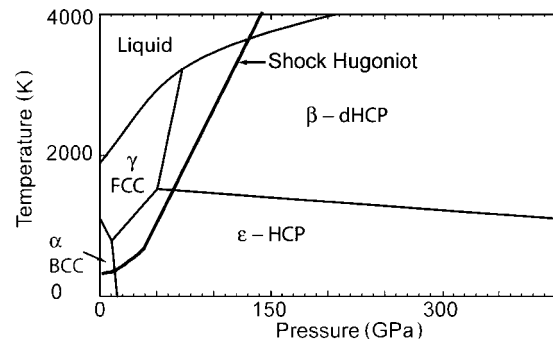

FIG. 1. The known phase diagram of iron under static conditions, from Saxena and Dubrovinsky (Ref. 10), with the shock hugoniot overlaid (Refs. 11 and 12).

the multiple waves seen in shocked iron, and that observed under static high-pressure conditions, are one and the same transition.

The shear stress experienced by crystals under the two different techniques can be radically different: in static measurements the crystals are compressed under hydrostatic conditions. In planar shock-wave experiments, the crystal sample is subjected to uniaxial strain. Hydrostatic conditions are approached only if significant plastic flow occurs (driven by the high shear stress) or if significant shear stress is relieved during a phase transition. Even then the material will retain some degree of shear stress due to the material strength. Thus, on the ultrafast time scale of a shock and before significant plastic flow occurs, there may be very significant differences between the conditions experienced by a shock loaded sample and hydrostatically compressed sample. These differences may well alter not only the path taken to the new phase, but perhaps the phase itself.

There is a long history of using x-ray diffraction to study and identify the phase of materials subjected to static compression.[14,15] For the case of iron, Mao and co-workers determined the lattice parameters of the bcc and hcp phases of iron as a function of static pressure up to 30 GPa.[16] Since that time, there have been numerous x-ray diffraction and extended x-ray absorption fine structure (EXAFS) studies of the transition under static compression.[16–19] Furthermore, an analysis of the observed c/a ratios has led to suggestions for the specific path for the transition—an important subject which we discuss later in this paper for shock compressed samples.

Given both the historical and scientific importance of the α-ϵ transition, *in situ* determination of the structure during shock compression is clearly of importance, and it is in this context that the recent direct confirmation of the shock-induced phase transformation by use of both nanosecond EXAFS,[4] and x-ray diffraction[3] should be viewed. In the work using nanosecond x-ray diffraction discussed here, iron is shown conclusively to transform to the hcp phase under shock compression.

This paper puts forward a fuller analysis of the experimental data and atomistic simulations than could be presented in Kalantar *et al.*[3] In particular, we provide a more detailed comparison of the experimental data with multimillion atom nonequilibrium molecular dynamics (NEMD) simulations,[20] and we show that uniaxial compression before the onset of the transition, the polycrystalline structure, and lattice orientation seen in those simulations are salient features within the experimental data.

The paper is arranged in the following manner. We first describe the possible mechanisms that have been suggested for the α-ϵ transition in iron under static compression, including how these mechanisms may be modified under conditions of an initial uniaxial strain. We then present a post-processed analysis of the NEMD simulations of the shock-induced phase transition, and associated simulated diffraction patterns. These simulated diffraction images, along with the direct information about atomic positions within the simulation, point to a particular mechanism for the transition under shock compression that differs from the suggested pathway under static compression.[19] We then present
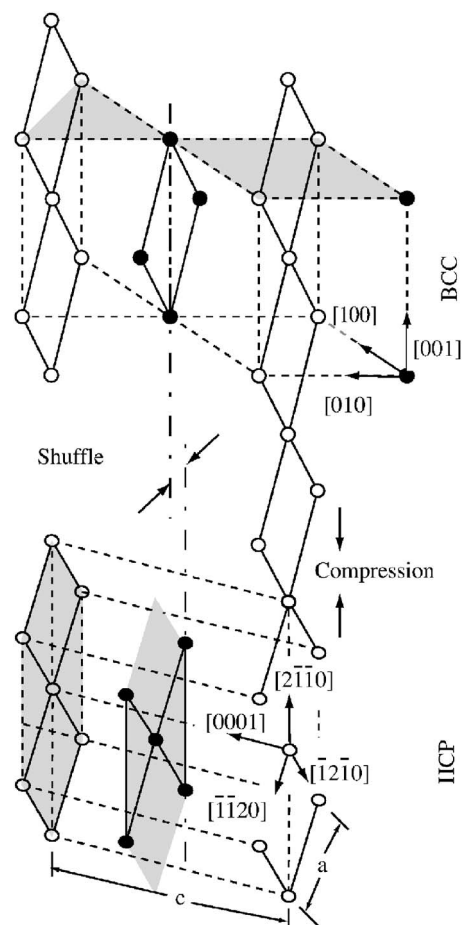

FIG. 2. A 3D perspective view of the α-ϵ phase transition in iron for mechanism I. This figure also provides the relative orientation of the bcc and hcp axis.

the experimental data showing how detailed fitting of simulated diffraction lines to the data restricts the possible paths by which the transition occurred. Finally, we discuss similarities between the NEMD simulations and the experimental data.

II. TRANSITION MECHANISMS FOR THE α-ϵ TRANSFORMATION UNDER HYDROSTATIC COMPRESSION

The kinematics of the iron α-ϵ phase transition under hydrostatic compression have been described by Wang and Ingalls.[19] They put forward three different possible mechanisms for the transition and discuss the consistency of each model with EXAFS measurements taken under hydrostatic pressures between 5 GPa and 18 GPa. We summarize these three mechanisms as mechanism I and mechanism II+IIa.

We then describe possible modifications to the mechanisms for the case where pressure is applied to the sample by shock loading. Figure 2 shows a three-dimensional (3D) perspective view of the phase transition and relative lattice orientations. This orientational relationship is used throughout the paper and for both transition mechanisms when discussing different hcp and bcc directions and planes.
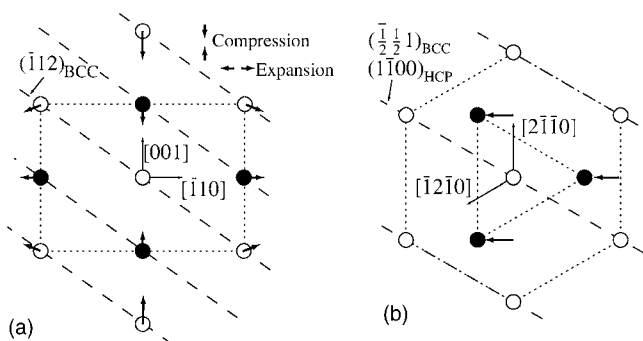
FIG. 3. Schematic diagram showing the transformation from (a) bcc to (b) hcp by mechanism I. The $(110)_{bcc}$ and $(0002)_{hcp}$ planes are in the plane of the paper. The hollow and solid circles denote atoms in the page and above the page, respectively. Arrows denote the direction of motion of the atoms. (a) defines the coordinate system in terms of the bcc indices and has arrows showing the expansion and/or compression and dashed lines indicating the location of the $(\bar{1}12)_{bcc}$ planes. (b) defines the coordinate system for the hcp and arrows showing the shuffle of atoms with the $(1\bar{1}00)_{hcp}$ planes labeled.

A. Mechanism I

The first proposed mechanism for the phase transition is a two step process. In the initial step the atoms in the $(110)_{bcc}$ plane are compressed along the $[001]_{bcc}$ axis and expand along $[\bar{1}10]_{bcc}$ to form a hexagon, as shown in Fig. 3. The second step is a shuffle of alternate $(110)_{bcc}$ planes in the $[1\bar{1}0]_{bcc}$ direction to create the two atom primitive cell. The resulting hcp structure has hexagonal planes—the $(0002)_{hcp}$ planes—corresponding to what were $(110)_{bcc}$ planes. Similarly, we find the $[2\bar{1}\bar{1}0]_{hcp}$ axis is aligned with the original $[001]_{bcc}$ axis, $[0002]_{hcp}$ with $[110]_{bcc}$ and $(2\bar{1}\bar{1}0)_{hcp}$ with $(002)_{bcc}$, as originally put forward in 1934 by Burgers.[21]

The rearrangement of the atoms for the bcc to hcp transition is illustrated in Fig. 3. This figure shows an important consequence of the shuffling of alternate $(110)_{bcc}$ planes that motivates using x-ray diffraction to determine the crystal structure. The shuffle causes a change in the stacking of the $(\bar{1}12)_{bcc}$ planes such that in the hcp phase these planes are effectively doubled in period. Thus the $(1\bar{1}00)_{hcp}$ plane corresponds to Miller indices of $(\frac{1}{2}\frac{1}{2}1)_{bcc}$, which will not diffract. Period doubling (due to the change from a monatomic to a diatomic primitive cell) is one of the hallmarks of the transition to the hcp phase, and thus diffraction from the $(1\bar{1}00)_{hcp}$ plane is one of the signatures used in diagnosing the existence of the hcp phase.

B. Mechanisms II+IIa

The other two models for the transition put forward by Wang and Ingalls are described here as II and IIa. These are also multistep processes: mechanism II is a two-step process, and mechanism IIa is a three-step process. However, both the initial step and the final structure are the same for the two
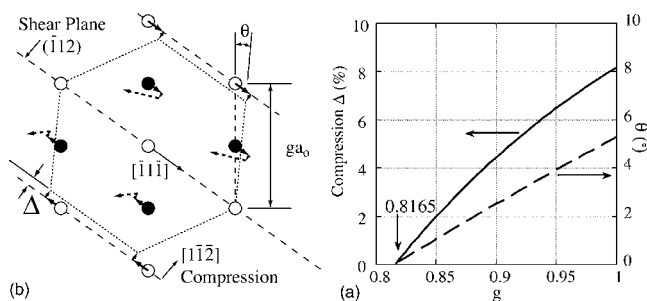

FIG. 4. (a) Schematic diagram showing the formation of hexagons in the $(110)_{bcc}$ plane for both mechanisms II and IIa (II' and IIa', see Sec. III). The $(\bar{1}12)_{bcc}$ shear plane, the $[\bar{1}1\bar{1}]_{bcc}$ direction, and the $[1\bar{1}\bar{2}]_{bcc}$ direction are labeled. The solid arrows denote the direction of the atomic motion due to the shear and/or compression. The dashed arrows represent the effective overall movement of the atoms when the crystal structure undergoes period doubling by mechanism II or IIa (II' and IIa'). (b) Rotation of the hcp unit cell, θ, and required compression along $[1\bar{1}\bar{2}]_{bcc}$ to form the hexagon in the initial step as functions of the initial elastic compression, g, where $g=1$ for hydrostatic conditions.

models and cannot be differentiated using x-ray diffraction, which is why we treat them together. The initial step of these two mechanisms is responsible for the motion of atoms within a bcc plane into a hexagonal arrangement, with the subsequent steps resulting in a shuffle, and lattice period doubling. The first step for these two models is illustrated in Fig. 4. Here, the atoms in the $(\bar{1}12)_{bcc}$ planes shear in the $[\bar{1}1\bar{1}]_{bcc}$ direction and compress in the $[1\bar{1}\bar{2}]_{bcc}$ direction. This results in a different orientation of the final hcp unit cell with respect to the initial bcc unit cell than found in mechanism I, which can be distinguished by x-ray diffraction.

We relate the motion of the atoms along $[\bar{1}1\bar{1}]_{bcc}$ to an angle θ, which is defined as the angle between the initial bcc state and the final hcp state. The motion along $[1\bar{1}\bar{2}]_{bcc}$ is the compression of the lattice described by Δ. In Fig. 4, the first arrow by the hollow atoms denotes the motion due to the shear and the second shorter arrow pointing towards the corners of the hexagon denote the motion due to the compression.

The hexagons formed by the shear and compression described above are slightly rotated about their c axes—i.e., about $[0002]_{hcp}/[110]_{bcc}$: for the case of hydrostatic compression it can be shown that to form hexagons in this manner, the hexagon is rotated by $\theta=5.3°$. Equivalently, the $(2\bar{1}\bar{1}0)_{hcp}$ plane will be at a $5.3°$ angle with respect to the original $(002)_{bcc}$ with overall compression of 8%. This angle depends on the amount of precompression of the bcc structure before the phase transition, and it is described by the factor g in Fig. 4, which is 1 for the hydrostatic case.

Once the atoms are arranged in hexagons, alternate planes shuffle to provide the period doubling. For mechanism II, this step is similar to the shuffle which occurs in mechanism I, i.e., alternate $(110)_{bcc}$ planes shift transverse to the loading direction, thus generating the final hcp structure.

The period-doubling process corresponding to mechanism IIa is different. In this case, it is proposed that the final hcp

phase is reached by motion of the atoms to create a meta-stable face-centred cubic (fcc) phase, and a further step is required to transform to the hcp phase. X-ray diffraction cannot differentiate the path of the shuffle because the end states are the same.

Wang and Ingalls state that mechanism IIa is preferred under hydrostatic conditions because the energetics are more favorable for the series of shear and slip systems, as opposed to a shuffle of alternate planes, that temperature dependent effects suggest a metastable fcc phase, and that passing through the fcc phase will generate a c/a ratio of 1.633 at the threshold for the transition, as observed in their experiments. The forces exerted on the sample in the hydrostatic and shock systems are completely different, and this will have consequences on the mechanics of the phase transition. We now discuss each of these mechanisms, constraining them to conditions seen in the experimental data, i.e., an initial uniaxial compression and no plastic flow.

III. PHASE TRANSITION UNDER UNIAXIAL SHOCK COMPRESSION ALONG $[001]_{bcc}$

In order to discuss the possible mechanism by which the transition occurred, and then to compare this mechanism with the hydrostatic case, we first consider the response of the shocked lattice in the absence of phase transitions. Below the Hugoniot elastic limit (HEL), a material responds in an elastic and reversible manner, without generating defects or dislocations. For a single crystal shocked along a principal axis, the atoms within the sample simply move closer to one another along the shock propagation direction. In particular, where the crystal is shocked along $[001]_{bcc}$, each of the cubic unit cells is compressed to become tetragonal—which we refer to as bcc cells compressed along $[001]_{bcc}$.

For shock pressures above the HEL, plastic flow occurs and a two-wave shock is formed. The precise mechanisms by which plasticity occurs—i.e., the detailed physics of the generation and propagation of dislocations, and the relevant time scales, are still a matter of considerable debate. As an example there is excellent evidence that in fcc materials, such as copper, plastic flow under shock compression occurs on time scales less than a nanosecond (as seen by experiment).[22] NEMD simulations suggest the time scales are actually much shorter—perhaps a few tens of picoseconds.[23] That said, little experimental or NEMD work has yet been performed on the elastic-plastic transition in bcc materials.

It is within this context that we identify a lack of plasticity under shock compression for bcc iron, both in the NEMD simulations that we show in Sec. V,[20] and in the experiment described in Sec. VI A.[3]

The impact of this lack of plasticity is that the mean spacing between the atoms in the direction orthogonal to the shock propagation direction cannot change. We discuss the mechanisms for the α-ϵ transition in this light in the following sections. A prime symbol is added to each mechanism to denote that atomic motion is similar to the hydrostatic mechanism (which are not primed) but with the added constraints of an initial uniaxial compression, i.e., starting the transformation from an initial state where $g < 1$, in Fig. 4.

A. Mechanism I′

Under the uniaxial strain conditions of a shock propagating along the $[001]_{bcc}$ direction mechanism I′ will again be a compression of the atoms in the $[001]_{bcc}$ direction, but with no expansion of the lattice in the $[\bar{1}10]_{bcc}$ direction. The hexagonal pattern in the $(110)_{bcc}$ plane must be generated simply by compression along $[001]_{bcc}$—this fixes the total compression to 18.4% with respect to the uncompressed bcc state. The second step of mechanism I′ is the same as its hydrostatic counterpart with alternate $(110)_{bcc}$ planes shuffling in the $[\bar{1}10]_{bcc}$ direction by $a_o/(3\sqrt{2})$. The resulting structure has a c/a ratio of $\sqrt{3}$ when a hexagon is formed in the $(110)_{bcc}$ plane. Above the transition, it is then possible to further compress the crystal, which will result in a distorted hcp structure.

B. Mechanism II′+IIa′

For mechanism II′+IIa′, the shear rotation angle, θ, and compression along the $[1\bar{1}\bar{2}]_{bcc}$ direction, Δ will be a function of the degree of shock precompression along $[001]_{bcc}$, g. This relationship is plotted in Fig. 4(b). In this figure, $g=1$ corresponds to the case where the lattice is initially uncompressed, similar to the hydrostatic case, whereas $g=0.8165$ corresponds to the case where the bcc lattice is compressed by 18.4%—i.e., mechanism I′, where no rotation of the lattice is required to produce a hexagon.

C. Degeneracy

In describing the possible mechanisms for the α-ϵ transition, we have referred to motion of atoms along specific sets of planes and directions. There is degeneracy in the planes and directions in which the atoms can move. However, not all planes in a family are equivalent. We describe the degeneracies that are present for this problem of shock compression of iron along the $[001]_{bcc}$ direction.

For mechanism I′, once the lattice has been compressed by 18.4% along the $[001]_{bcc}$ direction, the atoms form hexagons in the $\{110\}_{bcc}$ planes whose normal is perpendicular to the shock direction. There are four degenerate directions the $\{110\}_{bcc}$ planes can shift to cause the period doubling. Shuffling along the $[1\bar{1}0]_{bcc}$ and $[\bar{1}10]_{bcc}$ directions creates an hcp structure with the c axis parallel to the $[110]_{bcc}$ direction. The x-ray diffraction signal from both degenerate lattices is identical because the c axis is in the same direction. Alternatively, shuffling along the $[110]_{bcc}$ and $[\bar{1}\bar{1}0]_{bcc}$ directions creates an hcp structure with the c axis parallel to the $[1\bar{1}0]_{bcc}$ direction. The x-ray diffraction signal from these two degenerate lattices will also be identical, but different than the case where the c axis is parallel to $[110]_{bcc}$. These two possible orientations of the hcp lattice with respect to the bcc lattice are shown in Fig. 5. In the first case, Fig. 5(a), the shuffle of the atoms is along $[\bar{1}10]_{bcc}$, the c axis is out of the plane of the page (i.e., along $[110]_{bcc}$), and the hcp planes that correspond to the $(\bar{1}12)_{bcc}$ planes have doubled in pe-

FIG. 5. Degenerate lattice configurations showing the period doubling in the hcp lattice. (a) The case where the $(110)_{bcc}$ shuffle, and the spacing of the $(1\bar{1}00)_{hcp}$ plane is twice that of the $(\bar{1}12)_{bcc}$. (b) The case when the shuffle is into and/or out of the page and the spacing of the $(2\bar{1}\bar{1}2)_{hcp}$ planes is the same as the compressed $(\bar{1}12)_{bcc}$. These different lattice orientations can be resolved by x-ray diffraction.

riod, to become the $(1\bar{1}00)_{hcp}$ planes. Note, however, that what were the $(112)_{bcc}$ planes (not shown) are not doubled in period. In contrast, in Fig. 5(b) we show the positions of the atoms after forming the hexagon with a shuffle out of the plane of the page, along the $[110]_{bcc}$ direction. In this case, the c axis of the hexagon is in the plane of the paper—labeled $[0001]_{hcp}$. What were the $(\bar{1}12)_{bcc}$ planes have not doubled in period, and in the hcp system are labeled $(2\bar{1}\bar{1}2)_{hcp}$.

As these two sets of planes and shuffle directions are fully degenerate, we expect if the lattice rearranges under shock conditions by mechanism I′ a single crystal of iron transforming to hcp will contain equal numbers of these two types of "grains," with the c axis aligned along the original $[110]_{bcc}$ or $[1\bar{1}0]_{bcc}$ directions.

Similar degeneracies are also present for a lattice that rearranges via mechanisms II′ and IIa′. There are two possible

orientations for the c axis of the hcp lattice as for mechanism I′, and, for each of these orientations, the shuffle of alternate planes of atoms could occur in the positive or negative sense. However, there is a further degeneracy in mechanisms II′ and IIa′ in that the rotation of the hexagon around its c axis can be in either the clockwise or anticlockwise sense due to a shear along the $[\bar{1}1\bar{1}]_{bcc}$ or $[1\bar{1}\bar{1}]_{bcc}$ directions, respectively. Thus if the lattice transformed by mechanisms II′ or IIa′, there are four possible orientations of the hexagon with respect to the original bcc lattice which can be differentiated by x-ray diffraction.

IV. THE α-ϵ PHASE TRANSITION IN THE RECIPROCAL LATTICE

X-ray diffraction has been proven as an excellent diagnostic in determining the crystal structure of a material. We will show in Sec. V that we can calculate simulated x-ray diffraction patterns to interrogate the molecular dynamics simulations. To understand how to compare the reciprocal lattice to the x-ray diffraction data we look at the transformation of the reciprocal lattice similar to the physical space lattice in the previous section.

Figure 6(a) shows the reciprocal lattice of a perfect bcc lattice, with several points labeled. A line indicates the length of the $(\bar{1}12)_{bcc}$ reciprocal lattice vector. In Fig. 6(b) we show the reciprocal lattice for a perfect hcp crystal in the $[2\bar{1}\bar{1}0]_{hcp} \times [0\bar{1}10]_{hcp}$ plane, where the c axis of the hcp lattice is out of the plane of the paper. These points are labeled with Miller indices that correspond to the stated orientation. We also indicate those points that exist in a perpendicular slice in reciprocal space ($[0002]_{hcp}$ is in the plane of the paper) by a second lower set of labels. Note the period doubling in what was the $[\bar{1}12]_{bcc}$ direction.

FIG. 6. The reciprocal lattice of (a) bcc and (b) hcp. (a) The reciprocal lattice of bcc. This plane shows the points which fall on opposing corners and the one in the middle of the top and bottom faces of a cube in reciprocal lattice space. Some points have been labeled with their associated diffraction plane to provide an orientation. (b) The hcp reciprocal lattice showing the hexagonal base and the possible labels depending on the orientation of the hcp. For both plots the dimensions of k space are in units of $2\pi/a_0$, where a_0 is the lattice constant of the bcc unit cell.
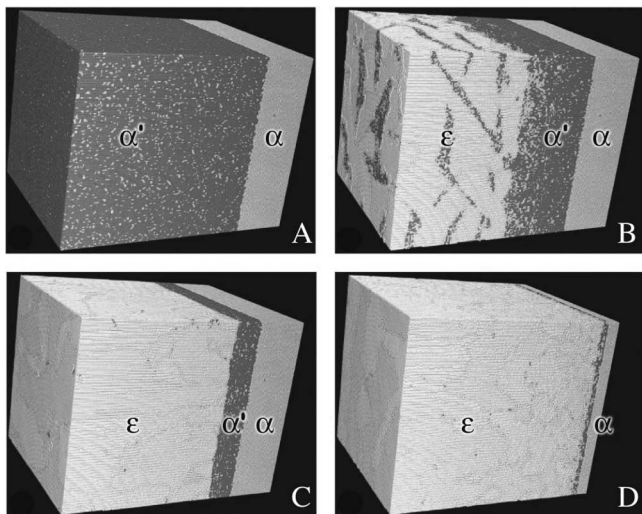
FIG. 7. Pictorial representations of the entire $40.2 \times 40.2 \times 57.4$ nm NEMD simulation for the four cases where the color coding corresponds to the number of nearest neighbors within a radius of 2.75 Å. Gray is uncompressed bcc, dark gray is uniaxially compressed bcc and light gray is hcp. The labels on the images correspond to the phase in that region. (Reprinted figure with permission from Ref. [20]. Copyright 2002 AAAS. URL http://www.sciencemag.org)

V. IRON NEMD CALCULATIONS

A. Description of the simulations

Having considered possible mechanisms by which single crystal iron may rapidly transform from a bcc to hcp structure under uniaxial shock conditions, we now turn our attention to large-scale NEMD simulations of this transformation. These simulations have been performed by Kadau *et al.*[20] Using the massively parallel NEMD code "SPaSM" ("scalable parallel short-range molecular dynamics"),[24] running on a 12-processor shared-memory Sun Enterprise 4000. Each simulation modeled 7.84×10^6 atoms in samples 57.4 nm long in the shock direction ($[001]_{bcc}$) and 40.2 nm in both the lateral directions ($200 \times 140 \times 140$ bcc unit cells).

The shock was generated using the momentum mirror method.[25] Atoms were specularly reflected by an infinitely massive, perfectly flat piston moving at velocity u_p, which generated a shock wave moving at velocity u_s. Periodic boundary conditions were applied in the lateral directions ($[100]_{bcc}$ and $[010]_{bcc}$). The duration of each simulation was <10 ps, approximately the time taken for the shock to transit the sample. Interactions between the atoms were modeled by use of the Voter-Chen embedded atom model (EAM) Fe potential.[26] This potential predicts the α-ϵ transition under shock compression at a pressure of just over 15 GPa, in reasonable agreement with the experimentally measured threshold pressure of ~ 13 GPa.[7,27]

Four simulations are studied with increasing piston velocities (u_p) as follows: **A** 362 ms^{-1}, **B** 471 ms^{-1}, **C** 689 ms^{-1}, and **D** 1087 ms^{-1}, as shown in Fig. 7. These velocities correspond to pressures along the shock propagation direction of 15.0 GPa, 19.6 GPa, 28.7 GPa, and 52.9 GPa, respectively. In Fig. 7 the atoms are color coordi-

nated according to the number of nearest neighbors within a radius of 2.75 Å, such that unshocked bcc appears gray, uniaxially compressed bcc appears dark gray, and hcp appears light gray (note that full color images of this figure can be found in the original paper, Ref. [20]).

B. Simulated x-ray diffraction from NEMD simulations

The NEMD calculations provide the coordinates of the iron atoms as a function of time as the shock propagates through the sample. We analyze the data in Fourier space, as this provides a direct correspondence with the experimental x-ray diffraction patterns discussed in the following sections. To generate the simulated diffraction patterns, we take the atomic data in real space, and generate a map in reciprocal space simply by taking a 3D Fourier transform of the atomic positions.[28,29]

$$F(\vec{k}) = \left| \sum_{j=1}^{N} e^{i\vec{k} \cdot \vec{r}_j} \right|^2, \qquad (1)$$

where N is the number of atoms and $\vec{r}_j$ is the location of the jth atom. This transform ignores the finite size of the atom (the atomic form factor), but this could be included by convolving the transform of the form factor with that of the lattice. However, the effect of this is to reduce the intensity of the scattering for high Miller indices. We have neglected this here.

As described in the previous section, the hcp phase occurs when hexagons are created from the $(110)_{bcc}$ or $(\bar{1}10)_{bcc}$ planes of the bcc lattice, either by direct compression along the $[001]_{bcc}$ direction as in Mechanism I′, or by a combination of rotation and compression, as in mechanisms II′ and IIa′. Thus we consider slices in Fourier space with orthogonal axes along the $[001]_{bcc}$ and $[1\bar{1}0]_{bcc}$ directions.

The atomic coordinates for the four simulations shown in Fig. 7 were postprocessed using Eq. (1) to generate simulated x-ray diffraction patterns. As described in Sec. IV, the diffraction planes correspond to points in reciprocal lattice space. The results of the $[1\bar{1}0]_{bcc} \times [001]_{bcc}$ plane are shown in Fig. 8. The calculated diffraction from simulation **A** shows only the bcc structure, i.e., a rectangular pattern with peaks that correspond to the corners and the center of the face of a cube. In this image each lattice peak is split in two, representing diffraction from both shocked and unshocked portions of the crystal in the simulation. The unshocked part of the crystal gives rise to the perfect bcc diffraction peaks, whereas the compressed crystal gives rise to peaks corresponding to a reciprocal lattice slightly expanded along $[001]_{bcc}$. We note that there is no shift of the diffraction spots in the $[1\bar{1}0]_{bcc}$ direction, confirming that the shocked crystal is elastically compressed in this simulation. The real lattice has been compressed uniaxially $7.0 \pm 0.5\%$.

Simulations **B**, **C**, and **D** have pressures that exceed the threshold for the phase transition. This is reflected in the reciprocal lattices shown in Fig. 8. We observe that each reciprocal lattice point from the original bcc crystal with a nonzero component along $[001]_{bcc}$ is split into three distinct

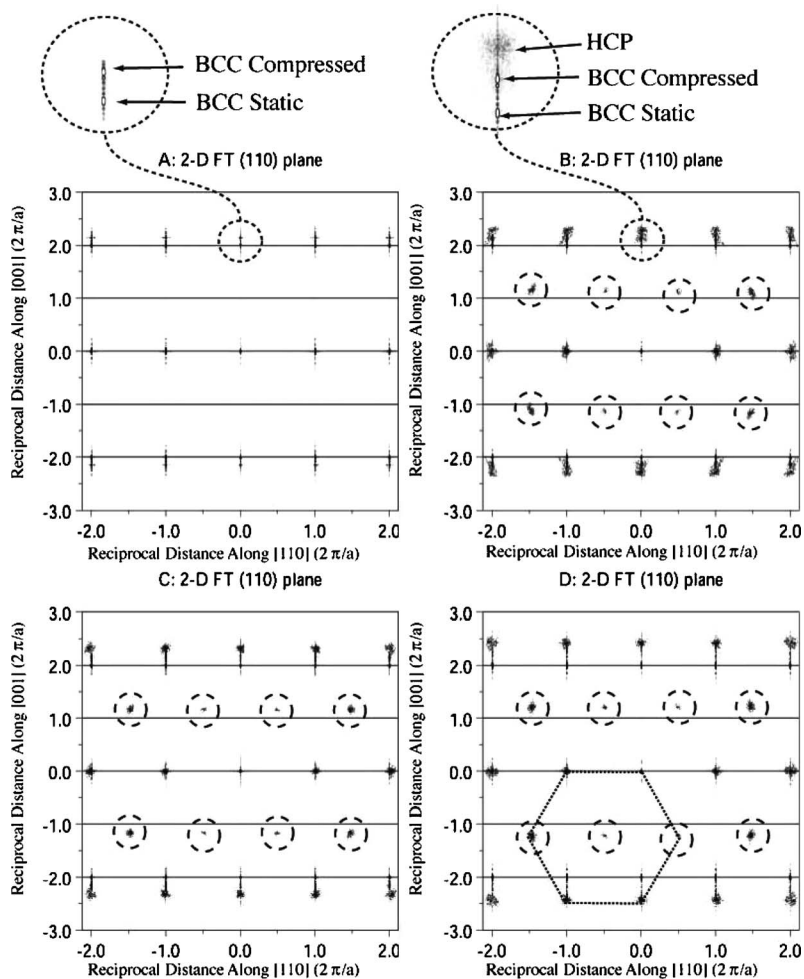FIG. 8. The $[001]_{bcc} \times [110]_{bcc}$ plane for the four MD simulations. Simulation **A** shows only the expansion of the bcc reciprocal lattice along the shock direction. **B**, **C**, and **D** show the formation of the hcp structure for 19.6 GPa, 28.7 GPa, and 52.9 GPa, respectively.

spots, corresponding to diffraction from the unshocked bcc lattice, the compressed bcc lattice, and a diffuse peak at an even higher compression. Additional diffraction spots in Fig. 8 **B**, **C**, and **D** indicated by dashed circles create a hexagonal pattern consistent with an hcp lattice. These are due to the period doubling of the $(\bar{1}12)_{bcc}$ planes. These new spots are not split, but are single spots, that occur above the threshold pressure where the additional diffuse peak is observed with the original bcc peaks. The presence of these diffuse points indicates that these simulations have undergone a change to hcp.

The relative intensity of the individual split spots [such as the $(002)_{bcc}- (2\bar{1}\bar{1}0)_{hcp}$ spot] varies according to the relative volume of material in the corresponding state. That is to say, for simulation **B**, about one half of the crystal is in the hcp phase, with the other half of the crystal almost equally divided between unshocked and shocked bcc material. At the highest pressure, simulation **D**, the diffraction from the hcp phase dominates the diffraction.

Analysis of the positions of the diffraction spots in reciprocal lattice space corresponding to the uniaxially compressed bcc lattice indicates that, as seen in simulation **A**, the lattice reaches a maximum uniaxial compression of 7.0±0.5% for all of the simulations. The peak corresponding to the hcp crystal shows a compression of the atoms which form the $(002)_{bcc}$ stacking by 11.5±0.5%, 13.8±0.5%, and

17.4±0.5% along the $[001]_{bcc}$ direction for simulations **B**, **C**, and **D**, respectively upon transition to the hcp phase. These compressions, deduced from the shift of the spots in reciprocal space, agree with the direct density measurements from the NEMD simulations, as shown Fig. 9.
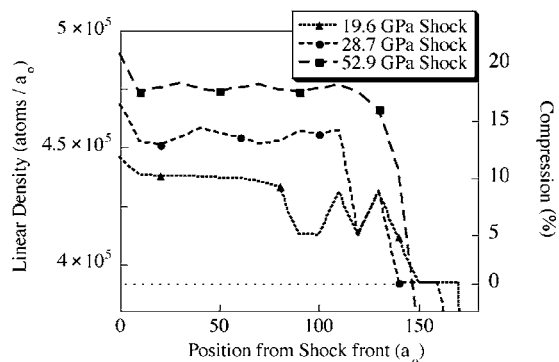

FIG. 9. The linear atomic density in the simulations plotted as function of position, showing compression that agrees with the simulated diffraction. There is an initial compression of ≈7% of the iron bcc lattice followed by a larger compression associated with the phase change to hcp. Note: the oscillation in the density are an artifact of the discrete atomic locations and the method used to create the bins.
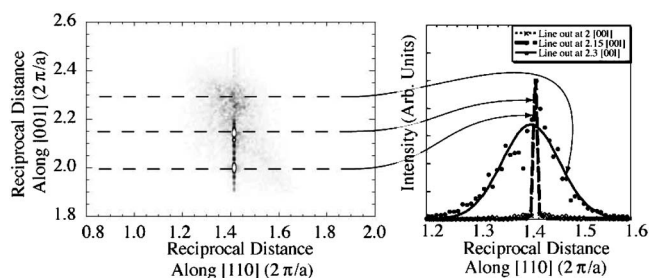
FIG. 10. Detail of the $(112)_{bcc}$ peak in reciprocal space sectioned through the $[001] \times [1\bar{1}0]$ plane for the 19.6 GPa compression. The lineouts show a more detailed location of the points along the $[1\bar{1}0]_{bcc}$ axis. There is a shift of the broad hcp peak suggesting a 0.7% lateral expansion.

The NEMD simulations show that with compression in the shock direction ($[001]_{bcc}$), only the highest compression of 52.9 GPa generates a structure which approaches an ideal hexagonal structure in the $(110)_{bcc}$ plane (i.e., approaching 18.4% compression). Looking at the reciprocal lattice in an orthogonal plane to the ones shown in Fig. 8 (i.e., the $[001]_{bcc}[110]_{bcc}$ reciprocal lattice plane), we find the identical pattern, suggesting that both orientations of the c axis of the hcp are present in the NEMD simulation, i.e., there are components of the crystal which have the c axis parallel to $[110]_{bcc}$ and others which are parallel to $[1\bar{1}0]_{bcc}$.

On the time scale of the simulations, there is no plastic flow in the NEMD simulated crystal. The generation and motion of dislocations associated with plastic flow would result in a reduction in the mean lattice parameter perpendicular to the shock propagation direction and an expansion of the reciprocal lattice. It is evident from all four plots that no perpendicular expansion occurs on these time scales for the compressed bcc and there are no significant dislocations observed in the real space images of the NEMD simulations Fig. 7. Figures 10 and 11 show an expanded view of the $(1\bar{1}2)$ point in reciprocal lattice space. The 19.6 GPa case shows no lateral deformation of the compressed bcc peak, i.e., no plastic deformation occurred before the phase change. There is a shift of the hcp peak corresponding to 0.7% expansion of the transformed hcp lattice perpendicular to the shock as determined by fitting a Gaussian profile to the broad
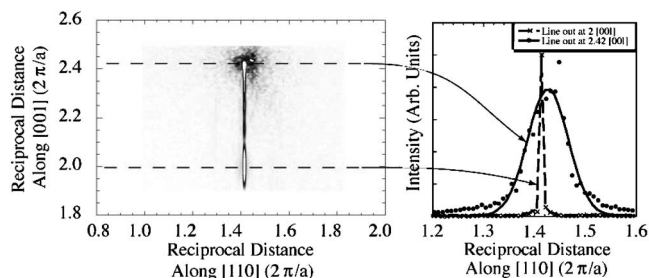

FIG. 11. Detail of the $(112)_{bcc}$ peak in reciprocal space sectioned through the $[001] \times [110]$ plane for the 52.9 GPa compression. The lineouts show a more detailed location of the points along the $[110]_{bcc}$ axis. There is a shift of the broad hcp peak suggesting a 0.7% lateral compression
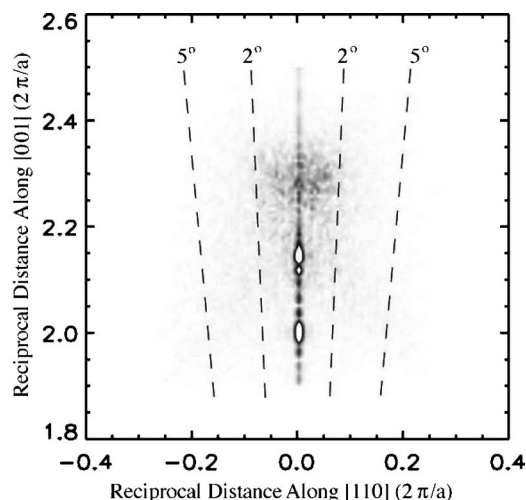

FIG. 12. A close up of the $(002)_{bcc}/(2\bar{1}\bar{1}0)_{hcp}$ diffraction plane in reciprocal lattice space in the $[110]$ plane. Angular contours are overlaid on to illustrate the effect of overall lattice rotation. The single diffuse spot $(2\bar{1}\bar{1}0)_{hcp}$ is consistent with no rotation of the lattice.

peak. Fitting the hcp peak for the simulation at 52.9 GPa peak pressure suggests that there is a 0.7% lateral compression of the atoms in the hcp phase. Note for this simulation that the small number of atoms in the uniaxially compressed bcc region and static bcc region cause the peak to severely broaden along the $[001]_{bcc}$ direction.

C. Possible mechanisms for the phase change

As described in Sec. III we can differentiate between the possible mechanisms for the phase change based on the orientation of the hcp lattice with respect to the bcc lattice [i.e., an angle between the $(002)_{bcc}$ and $(2\bar{1}\bar{1}0)_{hcp}$ planes]. A rotation of the lattice by 5.3° is an upper bound estimate of the rotation if the preferred pathway is mechanism II′ or IIa′, as it requires no precompression of the bcc lattice by the shock. The NEMD simulations predict a compression wave propagating through the bcc crystal, compressing it by 7%, before the transformation to an hcp-like structure. From Fig. 4(b), we see that for a perfect hexagon to be formed following the initial uniaxial compression, a rotation on the order of 3.5° would still occur.

A rotation in real space is evident in reciprocal space as a rotation in the pattern of peaks. In Fig. 12 we show an expanded view of the $(2\bar{1}\bar{1}0)_{hcp}/(002)_{bcc}$ spot in reciprocal space. Also shown on the plot are dashed lines oriented at ±2° and ±5° relative to the $[001]_{bcc}$ axis. With two possible directions that the rotation can occur we would expect to see the hcp feature composed of two spots, each slightly shifted off the axis. However, the spot is a single diffuse spot [of order ±1° full width at half maximum (FWHM)] centered along the $[001]_{bcc}$ axis. This suggests that the α-ϵ transition occurs by mechanism I′ in the NEMD simulations.

A similar conclusion is reached by an analysis of the positions of the atoms in the NEMD simulation in real space.
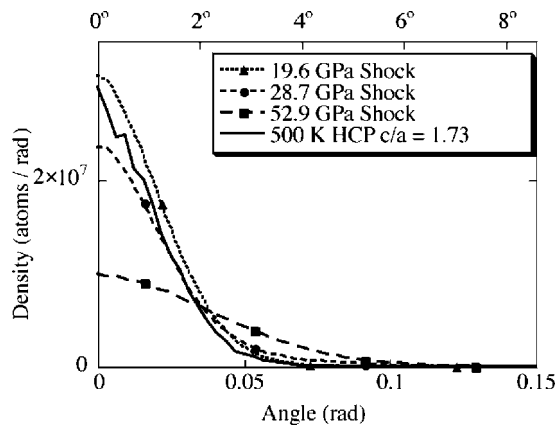
FIG. 13. Plot of the relative orientation of adjacent atoms relative to the shocked axis. The peak at 0 suggests that there is no rotation upon phase change in the simulation and the broadening is consistent with thermal broadening as shown by the plotting of a 500 K perfect hcp crystal.

The position of the closest neighboring atom in approximately the [001] direction was determined for every atom in the simulations in the hcp phase. A histogram of the angle between these pairs of atoms is plotted in Fig. 13. The angle between pairs of atoms in an unshocked compressed hcp sample at 500 K is plotted with the shock-compressed simulations to show the angular broadening is consistent with thermal fluctuations. This distribution peaks on the $[001]_{bcc}$ axis, indicating no overall lattice rotation. Again, this lack of rotation of the lattice suggests that mechanism I is the pathway for the transition.

VI. EXPERIMENT

A. Experimental setup

The experiments were performed using the OMEGA [15], Janus, and Vulcan [16] lasers. Samples of 200–270 μm thick single crystal [001] iron with a purity of 99.94% from Accumet Materials were coated with a 16–20 μm parylene-N ablator layer followed by a 0.1 μm aluminum shine-through layer. These samples were shock loaded by direct laser irradiation at 2×10^{10} to 1×10^{12} W cm^{-2} using 2–6 ns constant intensity laser pulses. The diameter of the region on the crystal shocked by the laser was determined by the laser focal spot size, and was of order 2–3 mm.

The shocked iron crystals were interrogated by wide-angle *in situ* diffraction, which has been described extensively elsewhere.[30–32] In this technique, a source of 1.85 Å iron K-shell x rays is created with additional laser beams focused on a metal foil synchronous to the shock-driving beams. X rays from a 100 μm−200 μm diameter source diffract from the surface of the crystal 0.7–1.3 mm away, and are recorded on a wide angle detector. For the 200 μm thick iron samples, the x-rays were diffracted from the shocked side of the iron crystal in reflection geometry—which we refer to as Bragg geometry. Additional experiments were conducted using 10 μm thick single crystal samples of iron. For these thinner samples it was also possible to perform
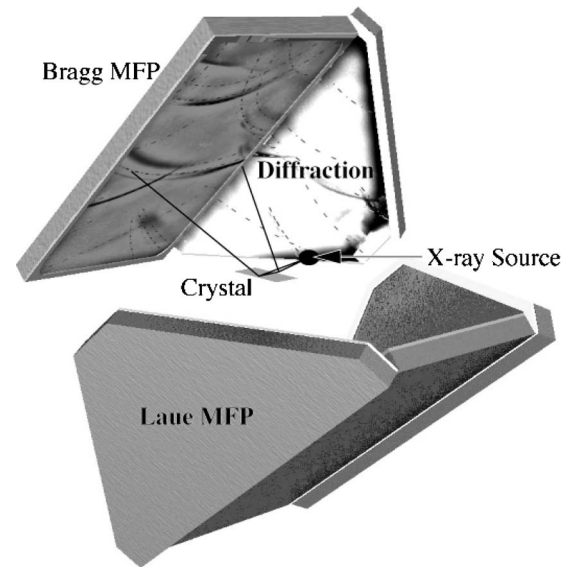

FIG. 14. Schematic diagram of the experimental setup. A point source of x rays is placed close to a single crystal. The diffracted signal from the crystal is recorded by wide angle film packs which can cover nearly 2π of solid angle. The film packs are placed to record reflected diffraction (Bragg geometry) and transmitted diffraction (Laue geometry).

diffraction in transmission geometry, which we refer to as Laue geometry. Due to the divergence of the x rays, and the large angle which the crystal subtends to the x-ray source, the x rays are diffracted from many different lattice planes in the crystal, resulting in multiple line features on the detector. Two wide angle multiple film packs (MFPs) covering a total of nearly 2π steradians recorded the diffracted signal in both Bragg and Laue geometry, as shown in Fig. 14.

B. Experimental results and analysis

The diverging quasimonochromatic point source of x rays covers a range of angles of incidence from $\approx 20°$ to $\approx 70°$ across the crystal surface, cylindrically symmetric about the x-ray source. X rays are diffracted from the crystal, and recorded on the MFP wherever the Bragg condition is met:

$$\lambda_o = 2d_{hk(i)l} \sin \theta,$$

where λ is the x-ray wavelength, $d_{hk(i)l}$ is the spacing of the $[hk(i)l]$ planes, and θ is the angle with respect to the plane from which the x rays are diffracted. Compression of the crystal results in changes in plane spacing $d_{hk(i)l}$ and normal directions, which in turn change the Bragg angle and shift the diffraction lines recorded on the film. On nanosecond time scales, the shock propagates through the parylene ablator and into the first few microns of iron. By varying the timing of the x-ray pulse with respect to the shock generation pulse x rays diffracted from unshocked material (ahead of the shock), shock-compressed bcc material, and (for high enough shock pressures) shock-compressed hcp material are recorded simultaneously.

Typical raw-data images from the MFPs are shown in Fig. 15. Figure 15(a) shows a diffraction pattern from both the
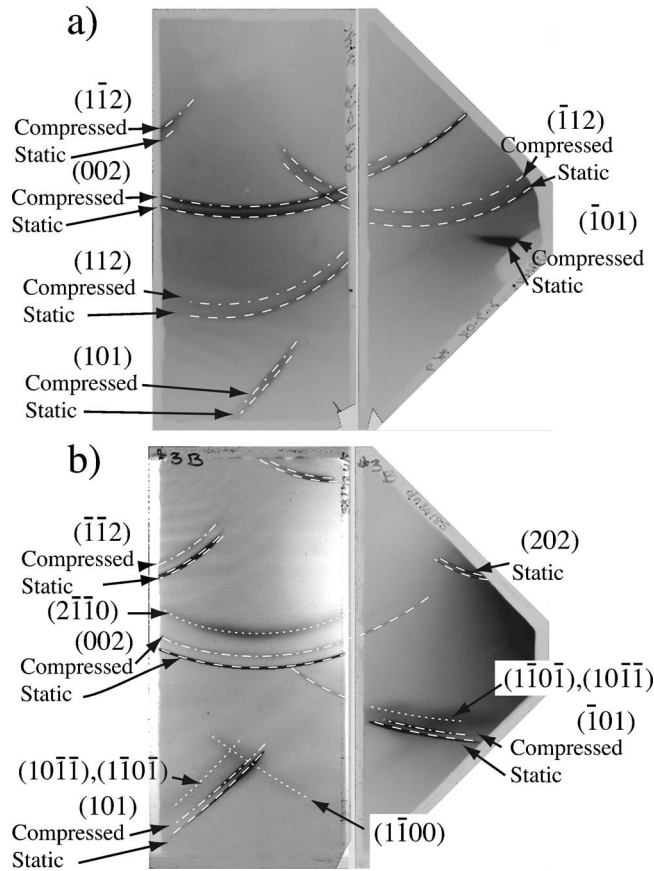
FIG. 15. Two complete data sets with the diffraction planes labeled with their Miller indices for both the bcc and hcp lattices. Note: the diffraction features that are due to degenerate planes are identified with labels associated with both possible hcp orientations. (a) Experimental data for a sample shocked at 5.4 GPa shows diffraction from static (dashed line), and 4.1% uniaxially compressed (dashed-dotted line) iron. (b) Experimental data for a sample shocked at 28 GPa the static (dashed line), 5.9% uniaxially compressed (dashed-dotted line), and ϵ phase (dotted line) are labeled.

shocked and unshocked bcc lattice on a single film at a pressure of 5.4 GPa, below that required for the α-ϵ transition. The diffracted x rays form arcs on the film. The location on the film and curvature of the arc gives information about the plane orientation and lattice spacing.[31] The Miller indices of the diffracting planes are shown for the raw data, both for the unshocked material (static) and shocked crystal (compressed). Figure 15(b) is a sample of raw data at a pressure of 26 GPa, above that required for the α-ϵ transition. Note that the arc corresponding to diffraction from $(002)_{bcc}$ is split into three components—the first corresponding to diffraction from unshocked bcc, the second to shock-compressed bcc, and the third to a further degree of compression which we have attributed to the hcp phase, as discussed below.

Analysis of the diffraction images is performed by comparing the experimental data to predicted patterns calculated by ray tracing. Within the ray tracing routine, the location and wavelength of the x-ray source, location and orientation of the crystal and crystal planes, and the location of the film are fixed. The location on the crystal surface where the Bragg condition is met is calculated for all possible diffract-

ing planes with $2d_{hk(i)l} \gg \lambda$. Then, knowing the location on the crystal from which the diffraction occurs and the relevant Bragg angle we calculate the location where the x rays are incident on the film. Compression and/or rotation of the lattice can be modeled. As the structure and lattice spacing of the unshocked crystal are known diffraction from an unshocked sample can be used to fit the relative location and orientation of the source, crystal, and detector.

Once the source, detector, and crystal positions and orientations have been identified, the compression and/or rotation of the unit cell of the crystal is modified in the ray tracing routine to determine the lattice parameters and orientation that best fit the diffraction lines from the shock-compressed crystal. For example, for the data shown in Fig. 15(a) at 5.4 GPa, we find that all of the diffraction lines can be well fitted assuming the compression along the shock propagation direction (i.e., $[001]_{bcc}$) is 4.1% ±0.3%. This compression is most easily inferred from the shift of the $(002)_{bcc}$ plane. This compression along $[001]_{bcc}$ also gives an excellent fit to the $(112)_{bcc}$ line of the shock-compressed crystal. As the plane has a component perpendicular to the shock propagation direction, this implies purely elastic compression of the lattice, as observed in the NEMD calculations.

Taking sample data at 12 GPa where the transition is observed, the best fit uniaxial compression from the diffraction lines associated with the $(002)_{bcc}$ plane is 5.2% ±0.2%. Assuming only uniaxial compression, the shift of the diffraction lines associated with the $(112)_{bcc}$ plane suggests 5.0% ±0.2% and the diffraction line associated with the $(1\bar{1}2)_{bcc}$ plane suggests 5.7% ±0.4%. Fixing the compression along the shock direction at 5.2% based on the change in diffraction of the $(002)_{bcc}$ plane, the lateral deformation can be estimated as a 0.3% ±0.5% expansion and 0.4% ±0.5% compression from the shift in the diffraction lines of the $(112)_{bcc}$ and $(1\bar{1}2)_{bcc}$ planes, respectively. A similar analysis of data recorded at 13 GPa shows compression in the shock direction of 5.8% ±0.3% with the lateral compression estimate of 0.3% ±0.6% expansion and 0.1% ±0.6% compression again for the change in the diffraction lines associated with the $(112)_{bcc}$ and $(1\bar{1}2)_{bcc}$ planes, respectively. Within the uncertainty of the measurement, there is only uniaxial elastic compression before the phase transition which agrees well with the MD simulations, even though the experimental time scale is orders of magnitude longer than the simulation.

This elastic response of iron above the HEL contrasts with the wave profiles of shocked iron observed on microsecond time scales.[7,33] In these longer time-scale experiments, a three-wave structure is often observed—the first being associated with the HEL, the second with an elastic-plastic transition, and the final wave associated with the phase transition itself. The laser experiments are at a time scale intermediate between the MD simulations and microsecond shock-wave experiments. The exact time scale for plastic behavior in shock-compressed iron thus remains an interesting issue.

At the lowest laser intensities, and thus the lowest applied pressures, only unshocked and elastically compressed bcc diffraction lines were observed. As the laser intensity, and thus shock pressure, is increased, the diffraction lines corre-

sponding to the shocked bcc indicate higher compressions. The pressure applied by the laser ablation of the plastic overcoat was not directly measured in these experiments. LASNEX was used to simulate the shock pressure for each laser experiment. These simulations provide an intensity scaling of the pressure but they are normalized by comparing with independent pressure estimates from third-order elasticity.[34] For the group of experiments where only uniaxial compression was observed, the simulated pressure was compared to that inferred from third-order elasticity. An average correction factor was determined and applied to the LASNEX simulated pressures for all experiments.

At the highest shock pressures a third line is evident in the diffraction associated with the original $(002)_{bcc}$ plane, as can be seen in Fig. 15(b). This third feature is observed only above a threshold pressure of approximately 13 GPa. It corresponds to a compression of the $(002)_{bcc}$ planes by between 15 and 18 %. This diffraction peak is broader and more diffuse than the peak associated with the unshocked lattice, and the compressed bcc lattice. The appearance of this third feature is correlated to additional diffraction peaks consistent with the period doubling of the $(\bar{1}12)_{bcc}$ plane in the Bragg geometry. This is labeled by its Miller indices $(1\bar{1}00)_{hcp}$ in Fig. 15(b). This type of period doubling is consistent with the shifting of alternate $(110)_{bcc}$ planes described earlier in Sec. II.

Due to the geometrical constraints of the experimental setup, there are only features consistent with one direction of the c axis associated with the hcp phase in Bragg reflection geometry. The transmitted Laue diffraction using thin crystals provides further information about the structure of the shock-compressed crystals. Figure 16(a) shows the diffraction in the Laue geometry when the crystal is shocked below the transition pressure. The overlaid lines and labels indicate the specific lattice plane Miller indices. In contrast, Fig. 16(b) shows the data for a crystal shocked above the phase transition. Note that two new diffraction lines appear corresponding to the $(0\bar{1}11)_{hcp}$ and $(0\bar{1}1\bar{1})_{hcp}$ reflections of the hcp phase, each consistent with a different orientation of c axis. The appearance of both of these reflections indicates that the single-crystal bcc lattice has transformed to an hcp structure with regions where the c axis is oriented along the original $[110]_{bcc}$ direction, and other parts where it is oriented along the original $[1\bar{1}0]_{bcc}$ direction, as described in Sec. II. The nearly equal intensity of the lines suggests that the amount of crystal in each orientation is approximately equal. The lines in Fig 16(b) have been labeled to distinguish between the two possible orientations of the hcp lattice.

The Laue diffraction also provides information about the atomic motion perpendicular to the shock. The locations of the lines are consistent with no lateral compression of the atoms upon the α-ϵ transition, although the width of the lines and nonuniformity of the thin samples makes it difficult to extract quantitative information. This suggests that the hcp lattice does not form a perfect hexagon in the $(110)_{bcc}$ plane. Instead, like the NEMD simulations the shift of atoms which cause the period doubling of the bcc lattice to make hcp occurs yielding an imperfect hcp lattice. The volume com-

FIG. 16. Data images showing the Laue diffraction recorded through a 10 μm single crystal iron sample shocked at a pressure of (a) 3.6 GPa where there is no shift in the diffraction planes perpendicular to the shock direction, and (b) at 13.8 GPa, above the transition threshold. The diffraction shows considerable broadening of the lines similar to the hcp lines identified in the Bragg geometry, plus the addition of two lines consistent with an hcp structure. The two different orientations are denoted by beginning the fitted line with "$\langle-\rangle$" arrows for one orientation "$\rangle-\langle$" for the other, and "$\times-\times$" for lines which are consistent with both. The labels are bracketed by the same symbol as the line to denote the label for a given orientation.

pression of the lattice is plotted as a function of shock pressure in Fig. 17. As both the shock-compressed bcc and hcp material are uniaxially compressed, the volume is simply proportional to the lattice spacing parallel to the shock direction. All measurements up to 6% compression are consistent with compressed $(002)_{bcc}$ planes with an uncertainty of approximately 0.3%. The measurements of 15%–18% compression, are consistent with the $(2\bar{1}\bar{1}0)_{hcp}$ planes with an uncertainty of approximately 1%–2%.

In this figure, we have made a distinction between the compressed bcc when it appears on its own (solid triangles), and when it appears simultaneously with the hcp feature (open triangles and open squares, respectively). If we interpret the observation of diffraction from both compressed bcc and the hcp as diffraction from a two-wave structure, similar to the NEMD simulations, then the pressure in the compressed bcc is not the peak applied pressure shown. Instead, the pressure in this first wave corresponds to the transition pressure. The maximum uniaxial compression of the bcc lattice is 6–7 %, consistent with a transition pressure of 13 GPa.[7]
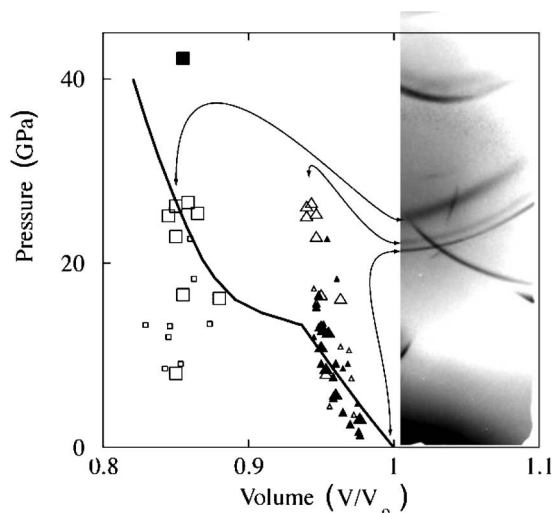
FIG. 17. Plot of the peak pressure vs volumetric compression calculated from the shift in the diffraction lines. The solid triangles represent measurements where only the compressed bcc line was present, the open triangles (bcc) and open squares (hcp) represent measurements made when both bcc and hcp were observed simultaneously. The solid square shows the case where only the hcp feature was observed. The symbols are shown in three different sizes for each shape, large denotes measurements made with a 351 nm drive, medium 532 nm drive, and small 1063 nm drive (note for the 532 nm drive only the compressed feature was observed). The room temperature shock Hugoniot is overlaid as a solid line.

C. The Mechanism

We will now evaluate the possible degree of rotation allowed within the experimental data and how that corresponds to the transition mechanisms described in Sec. II. Figure 18 shows the diffraction pattern from a 27 GPa shocked sample which has undergone the phase transition. Due to the degeneracy of the shift along the $\{110\}_{bcc}$ family of planes there are four variants of the rotation of the $(2\bar{1}\bar{1}0)_{hcp}$ plane. The Laue diffraction has shown that the transformed hcp crystal is polycrystalline suggesting that if mechanism II′ or IIa′ are responsible for the transition that all four rotations would have occurred. Fitting the hcp lines by different compressions for the four degenerate rotations is unphysical. We therefore compare the data with an overlay of the four rotations assuming a single compression. The relative shift of the four degenerate lines is shown in Fig. 18 assuming a 5° rotation of the hcp lattice upon phase change. This significantly over predicts the width of the diffraction lines.

As we see from Sec. III B, even if the bcc crystal is precompressed elastically by 6%, a rotation of 3.5° is still required by mechanism II′ or IIa′ to create a hexagonal structure. Figure 19 shows lineouts from the data with overlays of calculated line shape assuming all four degenerate lattice rotations exist. The arrows denote the center position of the diffraction lines. The simulated lineouts are broadened and scaled to obtain a best fit with the data. It is apparent that a rotation larger then 2° would not be consistent with the data.
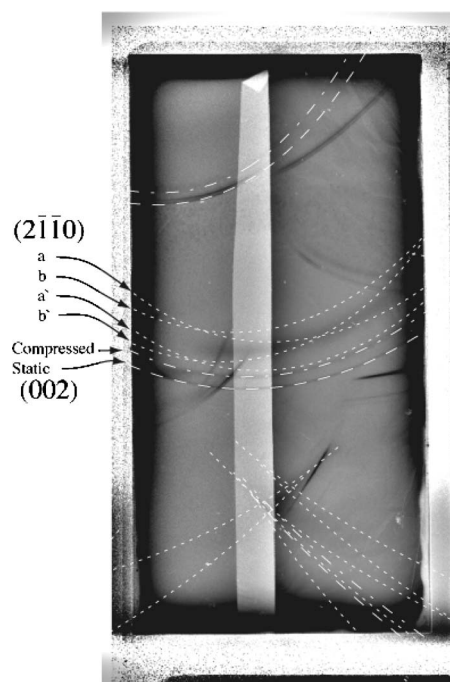
FIG. 18. Diffraction data image of a 27 GPa shock-compressed iron sample with overlaid lines accounting for the 5° rotation prediction assuming mechanism II′ or IIa′. The a and b denote the different hcp orientations. The prime denotes the −5° rotation for each of the orientations.

This rotation is too small for mechanism II′ or IIa′ even taking into account an unperfect hexagonal structure upon transformation. Thus we conclude that the experimental data is consistent with transformation mechanism I′.

D. Eliminating the possibility of an fcc structure

Based on the experimental data diffraction features observed upon shock compression indicate the hcp-like close-packed phase. However, iron also exists in the fcc (γ) phase over a wide region of temperatures and pressures, as indicated in the phase diagram shown in Fig. 1.

While iron does not pass through the γ phase on the Hugoniot, we consider the possibility that such a phase might be formed. Recent NEMD simulations indicate that a considerable fraction of shock-compressed single-crystal iron can transform to the γ phase if the crystal is shocked along the [110] or [111] directions.[35] Thus, before conclusively stating that the data confirms an hcp-like structure, it is important to eliminate the possibility that the data supports an fcc phase.

An fcc lattice can be generated by compressing along the $[001]_{bcc}$ axis to obtain a perfect hexagon in the $(110)_{bcc}$ plane, and then by shuffling pairs of $(110)_{bcc}$ planes in alternate directions to create the ABCABC… stacking of fcc with a cell size of $a_{fcc} = \frac{2}{\sqrt{3}} a_o$, oriented such that the hexagon is in the $(1\bar{1}1)_{fcc}$ plane, as shown in Fig. 20. The directions and planes of the fcc lattice that correspond to those in bcc are then $[110]_{fcc}$ with $[001]_{bcc}$, $(\bar{2}1\bar{1})_{fcc}$ with $(\bar{1}12)_{bcc}$, and

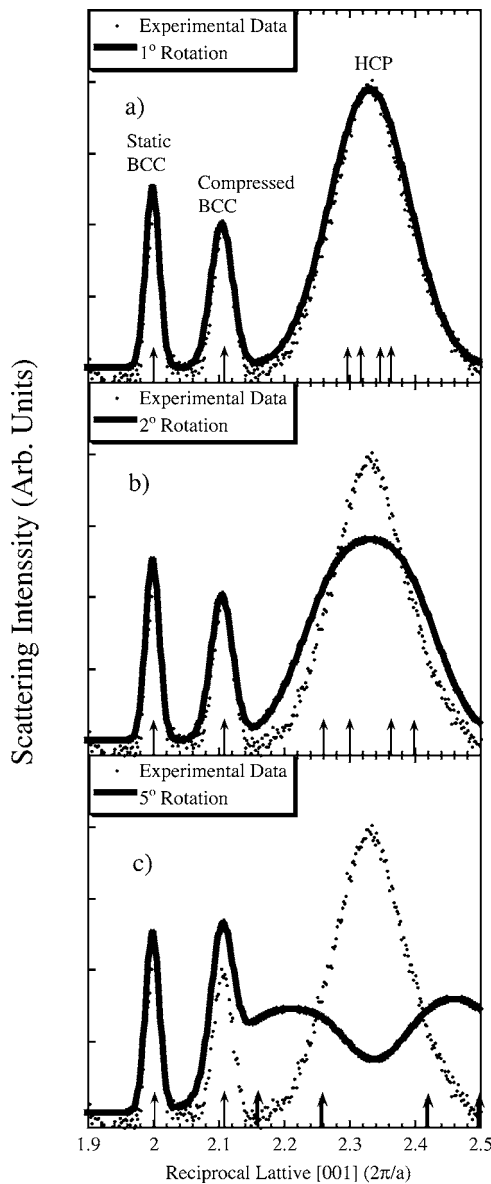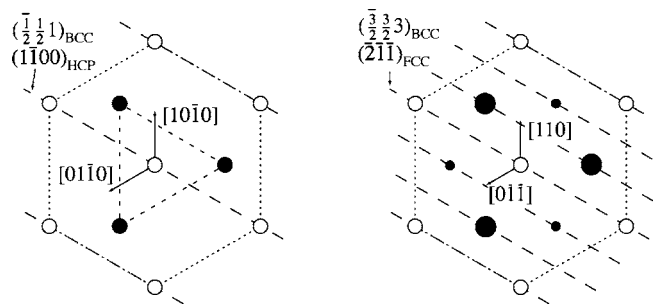FIG. 20. A comparison of the possible hcp and fcc end states. This shows the $(0002)_{hcp}$ or $(1\bar{1}1)_{fcc}$ plane. The atoms of different color and size denote different $(0002)_{hcp}$ or $(1\bar{1}1)_{fcc}$ planes. Note the hcp allows diffraction from the $(\frac{\bar{1}}{2}\frac{1}{2}1)_{bcc}$ plane where the fcc allows diffraction from the $(\frac{\bar{3}}{2}\frac{3}{2}3)_{bcc}$.

ing a rotation of the fcc lattice, the predicted diffraction for an fcc structure does not match these diffraction lines.

The fcc structure does not increase the number of diffraction lines relative to the bcc structure because both fcc and bcc have one atom per primitive cell. However, a transition from the bcc to fcc lattice will move the diffraction planes to new locations. One possibility to accommodate the appearance of new diffraction planes observed in the experiment is to generate period doubling by expand in volume by 21% in the transition from bcc to fcc. This would give agreement to the observed diffraction lines, but it is unphysical to have such a large expansion due to shock loading. As a result we conclude that the data supports the transition to hcp.

VII. DISCUSSION

In situ nanosecond x-ray diffraction was used to study the iron α-ϵ phase transition under shock compression in both experiments and NEMD simulations. Postprocessing the NEMD simulations with a Fourier transform effectively creates a simulated x-ray diffraction diagnostic allowing a direct comparison of the NEMD simulations with the experimental data. This type of postprocessing also gives the long-range

FIG. 19. Lineouts showing the compression of the $(002)_{bcc}$ lattice plane fitted by various degrees of rotation between the hcp and bcc lattices. At 2°, the width of the fitted line exceeds that of the experimental lineout. The vertical arrows denote the center position of each diffraction line.

$(220)_{fcc}$ will match $(002)_{bcc}$. Note that Fig. 20 also shows that the stacking of the fcc lattice is such that the $(112)_{bcc}$ plane becomes forbidden, as does the $(\frac{1}{2}\frac{1}{2}1)_{bcc}$ plane which corresponds to the $(1\bar{1}00)_{hcp}$ plane seen in Fig. 15.

Figure 21(a) shows the fitting of one diffraction image assuming an hcp lattice with only uniaxial compression, and no lateral movement other then the shuffle of the atoms. For all cases that show the period doubling this hypothesis fits the data very well.

The same data is fitted assuming an fcc lattice with its (220) plane parallel to the initial (002) plane. Figure 21(b) shows that the best fcc fit allowed by uniaxial compression does not match the lines we have identified with the hcp lattice, i.e., the $(1\bar{1}00)_{hcp}$ and $(10\bar{1}0)_{hcp}$ planes. Even allow-
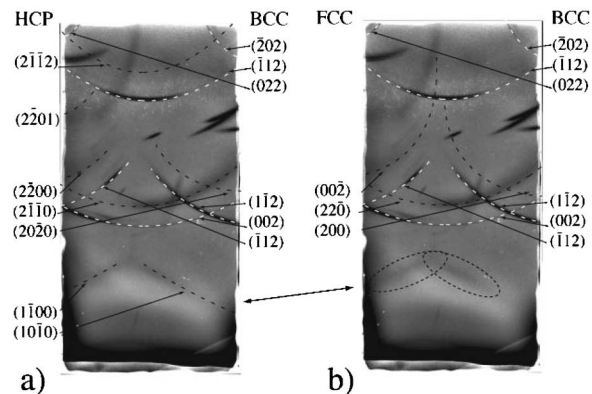

FIG. 21. Diffraction from a shock-compressed iron sample at 19 GPa fitted with (a) an hcp structure with the relations put forward by Burgers and (b) an optimum fit for the fcc.
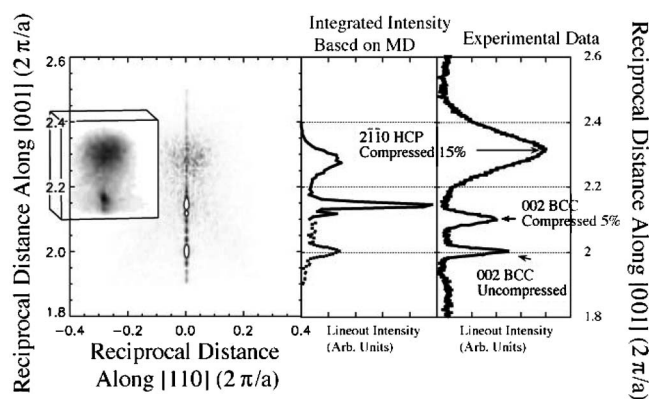
FIG. 22. Comparing the width of the peak from the postprocessed NEMD simulations and the experimental data. The far left is a 2D close up of the $(002)_{bcc}/(2\bar{1}\bar{1}0)_{hcp}$ spot with a 3D image inset. This is compared with a lineout from the experimental data converted to reciprocal lattice units.
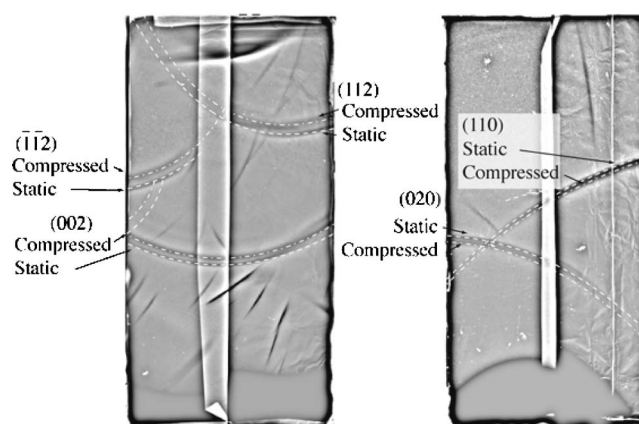

FIG. 23. Data images of Laue and Bragg diffraction taken simultaneously from the same iron crystal sample which was 10 μm thick, showing that there is some lateral compression of the lattice for some thin samples.

correlation between the atoms, to study the polycrystalline nature of the ϵ phase. The NEMD simulations and experiment both show the atoms undergoing an initial uniaxial compression before the α-ϵ transition, which requires a shift of alternate (110) planes. The simulation and experiment are both consistent with the transition occurring via mechanism I′, where compression along the $[001]_{bcc}$ direction generates a pseudohexagon in the $(110)_{bcc}$ plane with no rotation of the lattice. Overall, the agreement between the simulation and experiment is excellent even though the time scales are different by several orders of magnitude. Figure 22 shows the 3D Fourier transform (inset), a two-dimensional slice through the $(002)_{bcc}$ peaks, and the integrated projection on the $[001]_{bcc}$ axis of the NEMD simulation. This is compared with a lineout through the experimental data.

There is excellent agreement between the NEMD simulation and experiment. Both show sharp, well-defined bcc static and compressed peaks and a broad $(2\bar{1}\bar{1}0)_{hcp}$ peak. Note that the broadening of the simulated bcc peak is due to the finite number of atoms in the bcc state along the compressed direction, and the broadening in the experiment was limited by the finite width of the iron K-shell doublet used to probe the iron. The FWHM of the simulated $(2\bar{1}\bar{1}0)_{hcp}$ peak is 0.1 reciprocal lattice units while the experiment is 0.2. Different mechanisms for broadening of the hcp peaks are under investigation.

One interesting result that warrants further discussion is the uniaxial compression and lack of plasticity in the compressed bcc iron before it undergoes the phase change. Gas gun shock-wave profile measurements have shown the characteristic three wave structure associated with elastic and plastic compression and a phase change. Longer time-scale laser based shock-wave experiments also have shown features of a plastic transition on the order of 10 ns after the elastic wave.[36] Even the original Bancroft work resolved the three wave structure. There are many possible reasons why the elastic to plastic transition is not observed in the x-ray diffraction.

The diffraction probes $\approx$7 μm into the sample from the shocked surface. The gas gun work probed the free surface

which is on the order of a millimeter from the shocked surface, and the previous laser work looked over a 100 μm from the shocked surface. The diffraction suggests that at the driven surface there is no plastic wave, indicating that it requires a long distance in the sample to separate the plastic and phase transition waves to record each separately, as in the gas gun experiments. It may be that the transition from elastic compression to plastic requires a time scale which is too long compared to the time scale of the diffraction experiment (2 ns). Other drive techniques may offer a method to maintain the pressure on the sample for longer time scales in order to study the elastic-plastic transition in iron.[37,38]

The plastic effects may also depend on the sample itself. The characteristics of the original sample may affect its response to shock loading. Most previous work on iron samples was done with polycrystalline samples, while the diffraction experiments described here require single crystals. In these experiments, two types of single crystals where used, thick samples which where grown from a melt process, and thin samples which were vapor deposited onto a single crystal substrate. While the thin samples provide excellent qualitative Laue data they generally result in diffraction lines which are broken and difficult to fit assuming a perfectly flat single crystal. These thin crystals, are more susceptible to mechanical deformation from the handling required to assemble the targets. Bends in the crystals make regions of the sample diffract to different locations then expected on the film, at the microscopic level, the bending would lead to dislocation generation.

Figure 23 shows the diffraction pattern recorded at 11 GPa with a thin crystal. The hcp lines are not observed but the Laue pattern shows some compression perpendicular to the shock direction. The shift of a single line in the Laue film suggests a 2.4%±0.3% compression. In this case the lateral compression inferred from the $(\bar{1}\bar{1}2)_{bcc}$ is 2.3%±0.6% and from the $(112)_{bcc}$ plane is 2.8%±0.6%. Where the $(002)_{bcc}$ plane suggests a compression of 3.8%±0.2% along the shock direction, for a total volume compression of 9%±1%. While there was no characterization of the initial defects in this sample these results suggest

that understanding the elastic to plastic transition in iron requires further research, particularly understanding how the initial crystal state affects the response and final state.

Varying the defect density in the sample and the crystal orientation will provide more information about the iron α-ϵ-transition. This article is focused on compression of single crystal iron along a single crystallographic axis. Recent NEMD simulations suggest that by altering the shock direction, the material response at the atomic level changes.[35] By shocking along the $[110]_{bcc}$ or $[111]_{bcc}$ direction in the crystal the transition appears to favor the γ (fcc) phase over the ϵ (hcp). This presents an interesting question about the end phase for a given transition and what this would mean in a polycrystalline sample where the grains are oriented randomly with respect to the shocking direction. Continuing effort is being placed on simulation and experiment to understand the effect of shocking along different crystal axes.

*Electronic address: hawreliak1@llnl.gov

[1] P. W. Bridgman, *Collected Experimental Papers* (Harvard University Press, Cambridge, 1964).

[2] Michael I. Bergman, Nature (London) **389**, 60 (1997).

[3] D. H. Kalantar, J. F. Belak, G. W. Collins, J. D. Colvin, H. M. Davies, J. H. Eggert, T. C. Germann, J. Hawreliak, B. L. Holian, K. Kadau, P. S. Lomdahl, H. E. Lorenzana, M. A. Meyers, K. Rosolankova, M. S. Schneider, J. Sheppard, J. S. Stölken, and J. S. Wark, Phys. Rev. Lett. **95**, 075502 (2005).

[4] B. Yaakobi, T. R. Boehly, D. D. Meyerhofer, T. J. B. Collins, B. A. Remington, P. G. Allen, S. M. Pollaine, H. E. Lorenzana, and J. H. Eggert, Phys. Rev. Lett. **95**, 075501 (2005).

[5] J. M. Walsh, Bull. Am. Phys. Soc. **29**, 28 (1954).

[6] P. W. Bridgman, Proc. Am. Acad. Arts Sci. **74**, 11 (1940).

[7] D. Bancroft, E. L. Peterson, and S. Minshall, J. Appl. Phys. **27**, 291 (1956).

[8] S. Minshall, Phys. Rev. **98**, 271 (1955).

[9] P. W. Bridgman, J. Appl. Phys. **27**, 659 (1956).

[10] S. K. Saxena and L. S. Dubrovinsky, Am. Mineral. **85**, 372 (2000).

[11] J. C. Boettger and D. C. Wallace, Phys. Rev. B **55**, 2840 (1997).

[12] C. S. Yoo, N. C. Holmes, M. Ross, D. J. Webb, and C. Pike, Phys. Rev. Lett. **70**, 3931 (1993).

[13] J. C. Jamieson and A. W. Lawson, J. Appl. Phys. **33**, 776 (1962).

[14] Y. Z. Ma, M. Somayazulu, G. Y. Shen, H. K. Mao, J. F. Shu, and R. J. Hemley, Phys. Earth Planet. Inter. **143-44**, 455 (2004).

[15] J. F. Lin, O. Degtyareva, C. T. Prewitt, P. Dera, N. Sata, E. Gregoryanz, H. K. Mao, and R. J. Hemley, Nat. Mater. **3**, 389 (2004).

[16] H. Mao, W. A. Bassett, and T. Takahashi, J. Appl. Phys. **38**, 272 (1967).

[17] A. P. Jephcoat, H. K. Mao, and P. M. Bell, J. Geophys. Res., [Solid Earth Planets] **91**, 4677 (1986).

[18] W. A. Bassett and E. Huang, Science **238**, 780 (1987).

[19] F. M. Wang and R. Ingalls, Phys. Rev. B **57**, 5647 (1998).

[20] K. Kadau, T. C. Germann, P. S. Lomdahl, and B. L. Holian, Science **296**, 1681 (2002).

[21] W. G. Burgers, Physica (Amsterdam) **1**, 561 (1934).

[22] A. Loveridge-Smith, A. Allen, J. Belak, T. Boehly, A. Hauer, B. Holian, D. Kalantar, G. Kyrala, R. W. Lee, P. Lomdahl, M. A. Meyers, D. Paisley, S. Pollaine, B. Remington, D. C. Swift, S. Weber, and J. S. Wark, Phys. Rev. Lett. **86**, 2349 (2001).

[23] E. M. Bringa, J. U. Cazamias, P. Erhart, J. Stölken, N. Tanushev, B. D. Wirth, R. E. Rudd, and M. J. Caturla, J. Appl. Phys. **96**, 3793 (2004).

[24] D. M. Beazley and P. S. Lomdahl, Parallel Comput. **20**, 173 (1994).

[25] B. L. Holian and P. S. Lomdahl, Science **280**, 2085 (1998).

[26] A. F. Chen, S. P. Harrison, and R. J. Voter, in *Proceedings on Atomistic Simulation of Materials: Beyond Pair Potentials* (Plenum, New York, 1988), pp. 219–222.

[27] L. M. Barker, J. Appl. Phys. **46**, 2544 (1975).

[28] K. Rosolankova, D. H. Kalantar, J. F. Belak, E. M. Bringa, M. J. Caturla, J. Hawreliak, B. L. Holian, K. Kadau, P. S. Lomdahl, T. C. Germann, R. Ravelo, J. Sheppard, and J. S. Wark, *X-Ray Diffraction from Shocked Crystals: Experiments and Predictions of Molecular Dynamics Simulations* (Americal Institure of Physics, Melville, NY, 2004), Vol. 706, pp. 1195–1198.

[29] K. Rosolankova, Ph.D. thesis, University of Oxford, 2005.

[30] D. H. Kalantar, J. Belak, E. Bringa, K. Budil, M. Caturla, J. Colvin, M. Kumar, K. T. Lorenz, R. E. Rudd, J. Stölken, A. M. Allen, K. Rosolankova, J. S. Wark, M. A. Meyers, and M. Schneider, Phys. Plasmas **10**, 1569 (2003).

[31] D. H. Kalantar, E. Bringa, M. Caturla, J. Colvin, K. T. Lorenz, M. Kumar, J. Stölken, A. M. Allen, K. Rosolankova, J. S. Wark, M. A. Meyers, M. Schneider, and T. R. Boehly, Rev. Sci. Instrum. **74**, 1929 (2003).

[32] D. H. Kalantar, E. A. Chandler, J. D. Colvin, R. Lee, B. A. Remington, S. V. Weber, L. G. Wiley, A. Hauer, J. S. Wark, A. Loveridge, B. H. Failor, M. A. Meyers, and G. Ravichandran, Rev. Sci. Instrum. **70**, 629 (1999).

[33] E. A. Kozlov, I. V. Telichko, D. M. Gorbachev, D. G. Pankratov, A. V. Dobromyslov, and N. I. Taluts, Phys. Met. Metallogr. **99**, 300 (2005).

[34] A. D. Ritchie and M. W. Guinan, Ph.D. thesis, University of California, Davis, 1968.

[35] K. Kadau, T. C. Germann, P. S. Lomdahl, and B. L. Holian, Phys. Rev. B **72**, 064120 (2005).

[36] T. de Resseguier and M. Hallouin, J. Appl. Phys. **84**, 1932 (1998).

[37] K. T. Lorenz, M. J. Edwards, S. G. Glendinning, A. F. Jankowski, J. McNaney, S. M. Pollaine, and B. A. Remington, Phys. Plasmas **12**, 056309 (2005).

[38] J. Edwards, K. T. Lorenz, B. A. Remington, S. Pollaine, J. Colvin, D. Braun, B. F. Lasinski, D. Reisman, J. M. McNaney, J. A. Greenough, R. Wallace, H. Louis, and D. Kalantar, Phys. Rev. Lett. **92**, 075002 (2004).